Key Points:
- PKIIKP/PKIKP energy ratios are measured from a rare global data set of 33 antipodal seismograms
- PKIIKP/PKIKP energy ratios vary at short length scales (~200 km) along the inner core boundary, implying variations in shear velocity
- The presence of a nonuniform transition layer could explain lateral variations of shear velocity

Supporting Information:
- Supporting Information S1

Correspondence to:
J. Attanayake,
januka.attanayake@unimelb.edu.au

Irregular Transition Layer Beneath the Earth's Inner Core Boundary From Observations of Antipodal PKIKP and PKIIKP Waves

Januka Attanayake[1,2] (ID), Christine Thomas[1] (ID), Vernon F. Cormier[3] (ID), Meghan S. Miller[4] (ID), and Keith D. Koper[5] (ID)

[1]Institute of Geophysics, University of Münster, Münster, Germany, [2]Now at the School of Earth Sciences, University of Melbourne, Melbourne, Victoria, Australia, [3]Department of Physics, University of Connecticut, Storrs, CT, USA, [4]Research School of Earth Sciences, Australian National University, ACT, Australia, [5]Department of Geology and Geophysics, University of Utah, Salt Lake City, UT, USA

Abstract Standard Earth models assume a simple uniform inner core boundary (ICB) separating the liquid iron outer core from the solid iron inner core. Metallurgical and geodynamic experiments, however, predict lateral variations along this boundary originating from thermochemical and geodynamic instabilities during solidification. We search for evidence of this lateral heterogeneity by exploiting the sensitivity of antipodal PKIIKP waveforms to the shear wave velocity structure of the uppermost inner core beneath their reflection points on the underside of the ICB. Measuring PKIIKP/PKIKP energy ratios from 33 rare antipodal seismograms in the 178° to 180° distance range, we find this ratio varying between 0.1 and 1.1. Synthetic seismograms demonstrate that a laterally homogeneous liquid-solid ICB cannot account for this variability. Observations instead support a spatially variable ICB transition consisting of either (1) gradients in seismic velocities and density in which they smoothly increase from those at the outer core to those in the bulk of the inner core over a maximum depth of 10 km or (2) a layered transition with localized double discontinuities in velocities and densities separated by 4–10 km. A layered transition can generate a coda following PKIKP if shear velocity is small (<2 km/s) in the transition. Our results imply that the ICB is not uniform and might appear patchy with lateral rigidity variations. Nonuniform small-scale structural features that we infer to be present at the ICB are consistent with nonlinear solidification mechanisms driven by small-scale outer core convection in the lowermost outer core.

Plain Language Summary The Earth's core is divided into an outer liquid iron core and an inner solid iron core, where the latter freezes from the former. This growth process is not well understood because creating extreme physical and chemical conditions present in the deep interior in laboratories is difficult. Much of the knowledge about the inner core thus is indirectly obtained by modeling seismic waves traveling through it. Here we use a rare data set, where the seismic waves are recorded at stations nearly diametrically opposite to earthquakes, to constrain seismic structure near the inner core boundary. We find that amplitudes of waves that are reflected once from the underside of this boundary (PKIIKP) show rapid lateral variations relative to the waves that directly go through the inner core (PKIKP). We show that such variability can arise if the shear velocity structure—proxy to rigidity—in the vicinity of the inner core boundary is also varying. Our results, therefore, suggest that outer-to-inner core transition is not sharp but is characterized by a thin layer of varying rigidity and thickness. This indicates that the growth of the inner core is nonuniform and coupled to small-scale convection present at the bottom of the outer core.

1. Introduction

The solidity of Earth's inner core was confirmed by modeling normal modes sensitive to the inner core structure (Dziewonski, 1971), which led to the standard two-layer core model, in which solid inner core is separated from a liquid outer core by a sharp elastic discontinuity. The structure predicted from normal mode studies, however, is radially averaged over hundreds of kilometers. Information obtained from normal modes studies point to two puzzling features of the inner core: (1) the estimated Poisson's ratio (0.44) is significantly higher than that predicted from mineral physics experiments (0.32–0.38, Prescher et al., 2015) and is much closer to that of a liquid (0.50) than to a solid (0.25); and (2) the average shear wave velocity (V_s = 3.5 km/s) is much smaller than predicted in first principle calculations (4–7 km/s; Vočadlo, 2007).
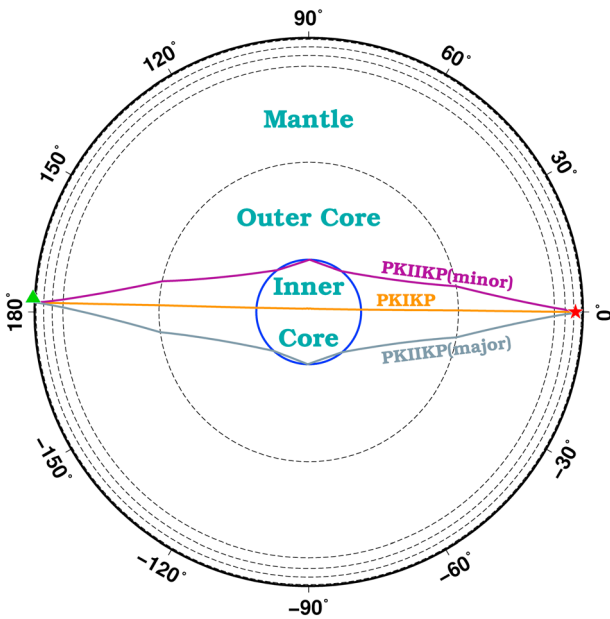
Figure 1. Antipodal raypaths for PKIKP (orange), PKIIKP minor arc (purple, $\Delta < 180°$), and PKIIKP major arc (gray, $\Delta > 180°$) phases. The star and the triangle symbolize the location of the earthquake and the recording station respectively. Major discontinuities in the Earth except the inner core boundary (blue solid line) are illustrated using black dashed lines. PKIIKP waves arriving within about 0.5° of the antipode from an impulsive source can hardly be separated into minor and major arcs as energy from all azimuths constructively interfere (Rial & Cormier, 1980). We do not have data within this critical distance bin.

Assuming a linear relationship between shear modulus, temperature, and pressure for extrapolation, Gleason and Mao (2013) predicted that bulk shear strength of hexagonally close-packed iron is naturally weak at inner core conditions. The application of linear extrapolation for the deep Earth, however, is a topic of debate (Martorell et al., 2016). Other hypotheses of presence of impurities such as carbon, partial melt, or mush in the inner core to explain these features also remain contentious (Chen et al., 2014; Deguen et al., 2007; Li et al., 2016) although some progress has been made more recently in predicting seismic velocities (e.g., Das et al., 2017).

Recently, Martorell et al. (2013) predicted that the premelting effect would exponentially reduce the inner core shear modulus above a homologous temperature of 0.96 if the medium were pure iron. This predicted homologous temperature is likely to be even smaller and spatially varying with the addition of impurities whose concentration itself might be spatially and temporally varying (Anderson & Isaak, 2002; Cottaar & Buffett, 2012; Gubbins et al., 2013). With this, Martorell et al. (2013) provide a mechanism to explain a *softer* inner core in addition to composition. If present, it is reasonable to assume that this effect is stronger near the ICB, where the liquid-to-solid transition takes place at a homologous temperature closer to unity. Seismic velocity and attenuation suggest that the thermal structure along the ICB might not be uniform, varying at both local and regional scale (Leyton & Koper, 2007; Stroujkova & Cormier, 2004), and global scale (Attanayake et al., 2014; Miller et al., 2013; Yu et al., 2017). Together with predictions of Martorell et al. (2013) and the geodynamic hypothesis of spatially varying heat flow at the ICB (Alboussière et al., 2010; Aubert et al., 2008; Gubbins et al., 2011; Monnereau et al., 2010), this implies that the medium immediately below the ICB might have a spatially variable shear modulus, resulting in variable $V_s$ possibly as low as zero at a homologous temperature of 1. Determining whether the inner core growth is nonlinear, as implied by a spatially varying shear modulus, is important for understanding the geodynamics of the deep interior.

Cormier et al. (2011) and Cormier (2015) demonstrated that the strong sensitivity of PKIIKP phase—a seismic wave that is reflected from the underside of the ICB (Figure 1)—to V_s at antipodal distances could be exploited to determine the V_s structure in the vicinity of the ICB. Theoretically, PKIIKP amplitudes are enhanced in the presence of a weak shear modulus at the ICB reflection point due to reduced efficiency of the *P*-to-*S* mode conversion (Figure 2). The transmission coefficient of PKIIKP at the ICB piercing points is little affected by a change in the shear modulus, minimizing the effect of structural heterogeneities at entry-exit points on wave amplitudes. Motivated by this prediction, we conducted a global search of PKIIKP waveforms at antipodal distances. Our objective was to determine if PKIIKP amplitudes exhibit discernible spatial patterns, implying lateral variations in the shear modulus. In addition, PKIIKP amplitudes allow us to constrain the shear modulus at the ICB reflection point and determine the nature of possible transition layers (Cummins & Johnson, 1988b; Deguen, 2012; Tian & Wen, 2017). In the next section, we describe methods used to analyze antipodal seismograms followed by details of data selection in section 3. We present our results in section 4, which are then discussed in section 5. Finally, we make our concluding remarks in the last section.

2. Methods

2.1. Processing Individual Seismograms

From our preprocessed data set of normalized seismograms (see details in section 3), we select those that were recorded at distances (Δ) ≥178° for further processing because optimum signal-to-noise (SNR) ratio of PKIIKP is expected in this distance range (Cormier et al., 2011). A crucial diagnostic feature of ICB conditions is the phase shift of PKIIKP waveforms (Cormier, 2015). In practice, observing phase shifts in PKIIKP waveforms can be challenging even at $\Delta \geq 178°$ due to interference of minor and major arc PKIIKP phases, and
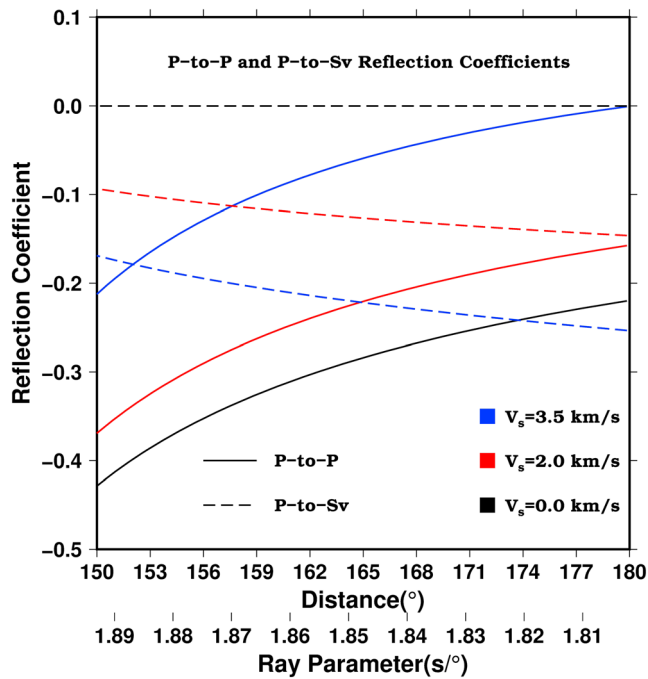
Figure 2. Reflection coefficients for far-field waves. *P*-to-*P* (solid lines) and *P*-to-*SV* (dashed lines) reflection coefficients are given in solid lines and dashed lines, respectively. Blue, red, and black curves are, respectively, for V_s = 3.5, 2.0, and 0 km/s beneath the inner core boundary. For the same distance, *P*-to-*P* reflectivity increases with reducing V_s in the inner core, whereas *P*-to-*SV* reflectivity decreases and is zero when V_s = 0. These calculations are based on Červeny (2001) and for the ak135 model (Montagner & Kennett, 1996).

interference of random noise when PKIIKP amplitudes are low. Instead, we find that total energy, defined as the area under a given wave in the envelope of a velocity seismogram, arriving with the PKIIKP pulse is a more robust observable. Therefore, we measure the energy ratio of PKIIKP to PKIKP and discard phase information.

We search for clear energy peaks associated with the theoretical arrival times of PKIIKP waves and then calculate residual differential travel times (DTTs) of PKIKP and PKIIKP arrivals with respect to Montagner and Kennett's (1996) ak135 model (i.e., observed DTTs − predicted DTTs). A cutoff residual DTT is applied to our data set of ±4 s, which is based on the expected travel time perturbation of a PKIKP wave at the antipode that samples the mantle and the anisotropic upper and lowermost inner core (Romanowicz et al., 2016; Wang et al., 2015). Perturbations to PKIIKP travel times due to inner core anisotropy, however, are not expected to be large because the bottoming depth of these waves at antipodal distances is at most about 80 km below the ICB, where the medium has largely been observed to be isotropic (Irving & Deuss, 2011; Song & Helmberger, 1995; Song & Helmberger, 1998). The ±4 s cutoff also eliminates the possibility of erroneously identifying the PKP-C$_{diff}$ wave as the major arc PKIIKP because PKP-C$_{diff}$ trails the major arc PKIIKP by about 10 s. Note that PKP-C$_{diff}$ is the wave that travels along the ICB on the liquid side and experiences sharp focusing near the antipode (Rial & Cormier, 1980). Following this selection, we measured PKIIKP/PKIKP energy ratios by integrating energy under respective pulses.

2.2. Seismic Array Processing

We also attempted to detect PKIIKP signals using seismic array processing techniques (Rost & Thomas, 2002, 2009) at a larger distance range (170° ≤ Δ ≤ 180°) than at the optimal narrow one selected in section 2.1. We processed 30 arrays with each array containing at least seven seismograms (505 seismograms in total), details of which are given in supporting information. Out of the 30 arrays we processed, no array contained robust signals of PKIIKP, that is, stable back azimuth and slowness estimates across three consecutive sliding windows in our slowness back azimuth analysis. Here we document four specific reasons for the nonobservation of PKIIKP phase in our data set.

First, a majority of our arrays are closer to 170° than to the antipode. In fact, 23 arrays were at a distance less than 175° (Figure S1). For these shorter distances, amplitudes of PKIIKP computed even for nonstandard Earth models are quite low (Cormier et al., 2011) and are possibly below the noise level.

Second, we detect persistent strong coda trailing PKIKP in some of the array beams we formed. The Baffin Bay-Antarctica raypath (Figure 3) provides an example of this. Here our slowness-back azimuth analysis and vespagrams (Rost & Thomas, 2002) show coda waves having a slowness similar to that of PKIKP persisting well past the minor arc PKIIKP. PKIKP energy *leaks* into the slowness range of PKIIKP, diminishing the detectability of PKIIKP.

Third, the significantly large azimuthal variation of stations within individual arrays located at distances greater than about 175° prevents us from stacking seismograms coherently. The variation in back azimuth in the 175°–178°can be up to 60°, and that for the array in the 178°–180° range is 176° (Figure S2). This large azimuthal variation violates the plane wave approximation on which our array processing method is designed, thereby introducing errors to estimated delay times. Future studies whose data exhibit similar spatial distribution might benefit from using array methods that delay-and-sum waves in Cartesian coordinate systems (e.g., Koper et al., 2003) rather than in spherical coordinate systems.

Fourth, travel times of higher-frequency waves could be perturbed by fine-scale 3-D heterogeneities in the inner core (to a greater degree) and mantle (to a lesser degree), hindering coherent stacking of seismograms in an array. This effect might be mitigated by low-pass filtering the data, in which case sensitivity to spatial
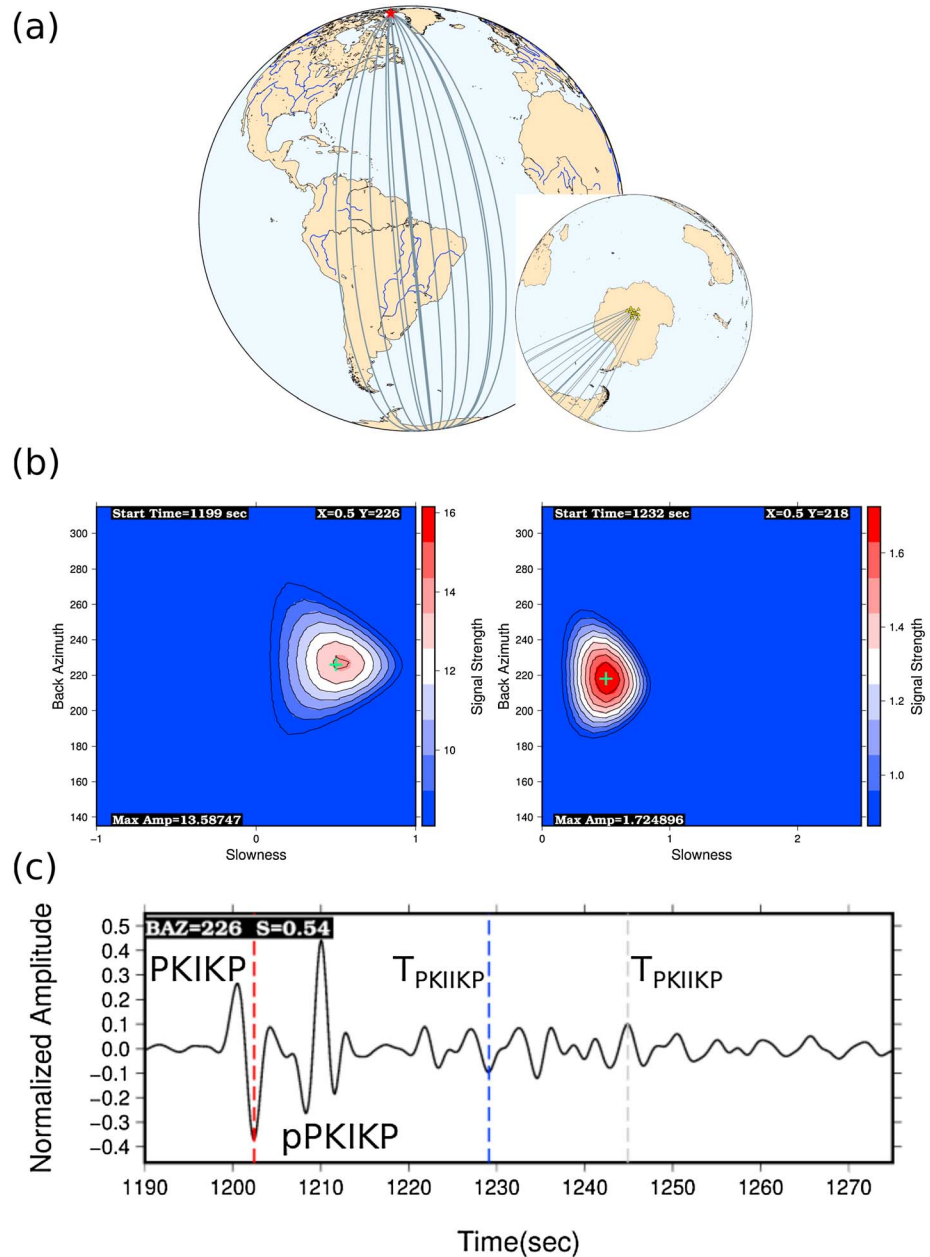
Figure 3. An example of array processing. (a) Earthquake location (red star), great circle raypaths (dark lines), and station array (inset). (b) Left: PKIKP signal detected with a slowness of 0.5 s/°and back azimuth 226°. The predicted back azimuth of this particular event-array combination is 224°. Right: PKIKP coda waves arriving with a slowness of 0.5 s/°and back azimuth 218°that mask the PKIIKP signal that has a predicted slowness of ±1.8 s/°. This coda energy is persistent, strong, and leaks into the PKIIKP slowness window. Note the difference in scales, indicating lower energy in the PKIIKP time window. (c) Beam-formed seismogram using optimally determined back azimuth (226°) and slowness (0.54 s/°). The dashed lines indicate the predicted arrival times of PKIKP (red) and PKIIKP phases (blue and gray) with strong PKIKP coda waves imaged in PKIIKP time windows, masking PKIIKP waves.

heterogeneities that we investigate in this study is lost. For example, Niu and Chen (2008) measured travel times of PKIKP and PKIIKP waves from array data recorded at ~176° by applying a low-pass filter with a corner at 0.5 Hz. Note that the Fresnel zone diameter of a PKIKP wave at 0.5 Hz is ~400 km, whereas it is ~850 km at 0.125 Hz (Kvasnička & Jansky, 1999). Given that Niu and Chen (2008) were able to coherently stack near-antipodal waves, it seems that the ICB would appear uniform to these waves at spatial scales larger than ~400 km. Nonetheless, *N*th-root stacking they required to extract signals and measure travel

times has the undesirable effect of distorting waveforms (McFadden et al., 1986), which would render energy ratios inaccurate. For this reason, we do not use Nth-root stacking. In fact, using lower-frequency bands with linear stacking did not improve beam forming in our case.

3. Data

PKIIKP waveforms are more likely to be observed at near antipodal distances, although recordings at these distances are rare due to limited source-receiver combinations. Only two source-receiver pairs are known to record seismograms consistently at $\Delta \geq 175°$: South America to East Asia and Tonga to West Africa. Keeping this in mind, we conducted a global data search from 1 January 2000 to 31 December 2016 (17 years) of individual and array recordings to include these known combinations as well as a few other crucial, different raypaths.

Our criteria for downloading data were as follows: $170° \leq \Delta \leq 180°$, $6.0 \leq$ magnitude $(M_w) \leq 7.8$, 0 km $\leq$ earthquake depth $\leq$ 700 km, and preliminary SNR > 1.25. From this initial data set of 1,346 events, we created a subset of 62 events that generated at least one seismogram at $\Delta \geq 178°$ and at least 10 seismograms in the 170°–180° distance range. The condition for a total number of seismograms was imposed as a preemptive measure to ensure the quality of data and as a requirement for seismic array processing. To increase the volume of our array data set, we also incorporated seismograms recorded by 3-D, XB, and Portuguese arrays located in Northern Africa and Western Iberia, although the condition of having at least one seismogram above a distance of 178° was not met for the events selected for these networks. This added another 15 events to our data set. Additionally, we supplemented our data set by incorporating seismograms from four events reported by Butler and Tsuboi (2010) for the Tonga-West Africa path, and seismograms from a rare 620-km deep event beneath Spain recorded by a seismic network in New Zealand. This Spain-New Zealand array recording was indeed unique because it contained the most number of seismograms (11) above the desirable Δ of 178°. In addition to these, we also found another rare antipodal path: An event located in Baffin Bay in the North Atlantic recorded in Antarctica.

We standardized our data in a preprocessing step, where we deconvolve the instrument response, convert to particle velocity, and remove the mean and trend. After decimating the sampling period to 0.05 s, we normalize the traces by peak-to-trough amplitude of the PKIKP phase when PKIKP is clearly detectable. We discard seismograms that do not show a clear and simple PKIKP waveform due to source complexity, low SNR, or station defects. Finally, we apply a low-pass Butterworth filter to data with a corner at 1 Hz to reduce the effect of high-frequency near-surface noise and to allow for synthesizing high-frequency antipodal seismograms accurately. We process all seismograms recorded at $\Delta \geq 178°$ individually because detectability of PKIIKP is optimum in this particular distance range (Cormier et al., 2011), and then, when a sufficient number of stations (>7) are available per event, we apply array-processing techniques.

4. Results

In total, we processed 67 individual envelopes at $\Delta \geq 178°$, out of which 18 envelopes (27% of the data set) were discarded for not having clearly identifiable simple PKIKP waveforms. From the remaining 49 envelopes, 34 contained clear energy peaks associated with PKIKP and PKIIKP arrival times, whereas the other 15 (31% of the data set) did not exhibit clear PKIIKP energy peaks and were also discarded, reducing our data set to 34 energy envelopes (Table S1). From this data set, 18 contained interfering minor and major arc PKIIKP phases, 8 contained either the minor arc or major arc PKIIKP, and another 8 contained distinct minor and major arc PKIIKP phases free of interference, bringing the total number of PKIIKP/PKIKP energy ratio measurements to 42 (Figure 4).

In Figure 5 we show the two cases where minor and major arc PKIIKPs interfere (Figure 5a) and when they are distinct (Figure 5b) along with measured PKIIKP/PKIKP energy ratios. The differential travel time residual maps corresponding to Figure 5 are included in supporting information (Figure S3). The interference is usually observed when respective phases are separated by less than ~5 s. This observation can be explained by considering event depths less than 15 km, and the typical length (~5 s) of source time functions in our event list. For source-receiver combinations greater than ~178.5°, minor and major arc PKIIKP phases interfere with each other regardless of the depth of the event or length of the source time function. The minor arc PKII KP ray coverage of our data set is widely sampling the Pacific and East Asia, whereas that of the major arc
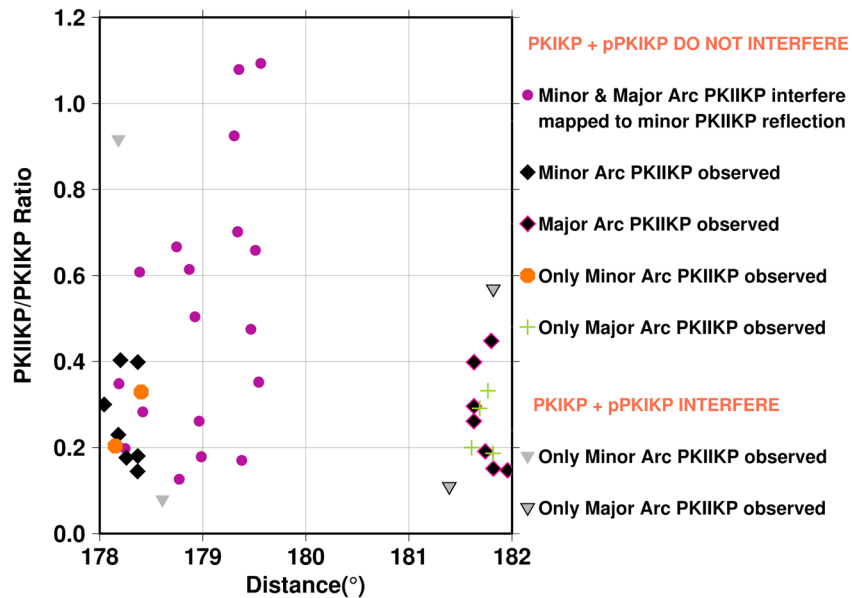
Figure 4. PKIIKP/PKIKP energy ratio with great circle arc distance (Δ°). Measurements at Δ ≥ 180°are major arc ones. Minor and major arc PKIIKP phases interfere with each other at Δ ≥ ~178.5°, and these have been mapped on to minor arc distances (i.e., Δ ≤ 180°).

covers Africa and the Southern Indian Ocean. The travel time residuals are within the expected scatter of ±4 s (see section 2.1) in our data set.

In Figure 6 we show PKIIKP/PKIKP energy ratio and differential travel time residuals versus the angle between the tangent to the ray at the bottoming point and the Earth's rotation axis (henceforth ray turning angle). Note that for data points where minor arc PKIIKP interferes with major arc PKIIKP, the time residuals were calculated with respect to the predicted times of minor arc PKIIKP. Thus, some unaccounted uncertainty might exist in the time residuals, and it is within the ±4 s threshold. As can be seen in Figure 6, we do not have any ray coverage below a ray turning angle of 30°, where strong anisotropy is predicted in the upper inner core (Romanowicz et al., 2003). Separately, anisotropy in the innermost inner core, where the symmetry axis varies between different models (Niu & Chen, 2008; Romanowicz et al., 2016; Wang et al., 2015), could potentially affect the PKIKP amplitudes in the 45°–90° ray turning angle range. A systematic variation of PKIIKP/PKIKP energy ratios or differential travel time residuals in this range, however, are not observed, suggesting that either the effect of anisotropy in the innermost inner core is not discernible in our data set or that the symmetry axis in the innermost inner core anisotropy is not distinct from that in the upper inner core.

We find in our numerical experiments (see section 5) that the predicted PKIIKP/PKIKP energy ratio for ak135 model at 179.5° is <0.1 for an explosion source, whereas our PKIIKP/PKIKP energy ratios vary between 0.1 and 1.1. Four of our measurements exceed 0.9, of which three are interfering minor and major arc PKIIKPs, and the other is a minor arc PKIIKP whose PKIKP phase interferes with its depth phase. When one considers the minor or major arc PKIIKP/PKIKP energy ratios free of interference, they are distributed between ~0.1 and ~0.5 except for the minor arc measurement mentioned earlier. All but two of our differential time residuals are scattered between +2 s and −3 s, which is consistent with travel time perturbations of PKIKP phases previously observed at antipodal distances in the quasi-equatorial plane (Romanowicz et al., 2016). It is reasonable to assume that the likely origin of travel time residuals we observe is primarily cumulative travel time perturbations of the PKIKP phase in the deeper inner core. We conducted tests of theoretical travel time calculations to better understand the effect of near ICB structure. For instance, PKIKP travel time from a 500-km deep earthquake at Δ = 179° increases only by 0.06 s, and that of PKIIKP by only 0.35 s if we model the uppermost 10 km of the inner core as a gradient. In this model, *P* and *S* wave velocities linearly increase from outer core to those of the inner core. Hence, the travel time differences due to changes in structure in the uppermost 10 km of the inner core are too small to explain the scatter in differential travel time at antipodal distances. We conclude that the observed travel time scatter must originate deeper in the inner
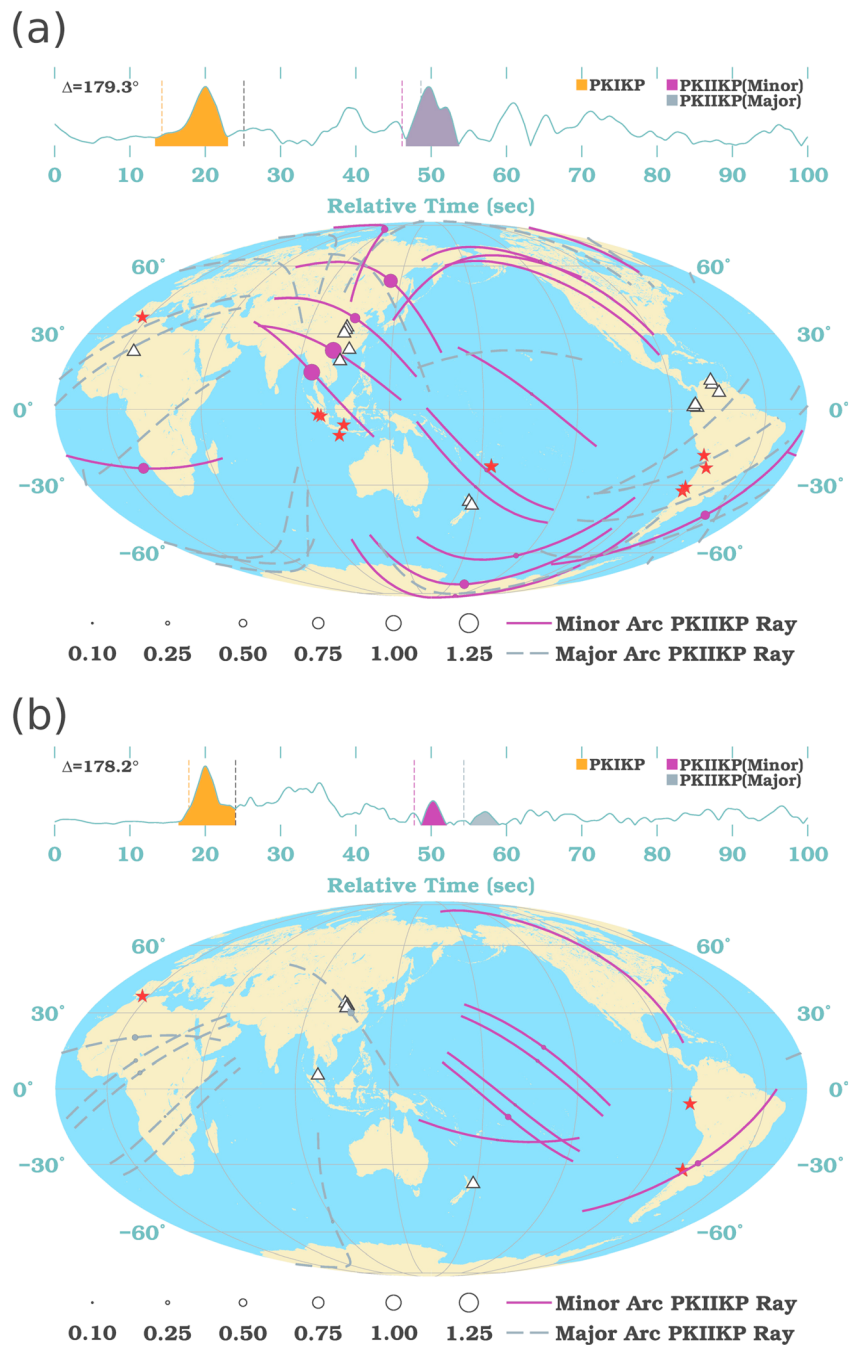
Figure 5. PKIIKP/PKIKP energy ratio, ray coverage, and typical envelopes for two different types of interference of phases observed in data. The energy ratio is mapped on to the reflection point as circles whose radii are proportional to the measurement (see scale). The ray segments in the inner core of PKIIKP phases are represented by solid lines. (a) PKIKP and pPKIKP do not interfere but minor and major arc PKIIKP interfere. Note the arrival of PKP-C_{diff} wave at ~60 s. (b) None of the phases interfere. Stars and triangles are earthquakes and stations, respectively. The dashed vertical lines on the envelopes show theoretical arrival times of PKIKP (orange), minor (purple) and major (gray) arc PKIIKP, and pPKIKP (black).

core and is a cumulative effect. Note that variations of this gradient model are used in section 5 to explain the distribution of PKIIKP/PKIKP energy ratios.

We do not observe a discernible spatial pattern either in PKIIKP/PKIKP energy ratios or differential time residuals (Figure 7). Regions showing higher-energy ratios (or differential time residuals) are interspersed with those showing lower ones. Note that when minor and major arc PKIIKP phases interfere, data points
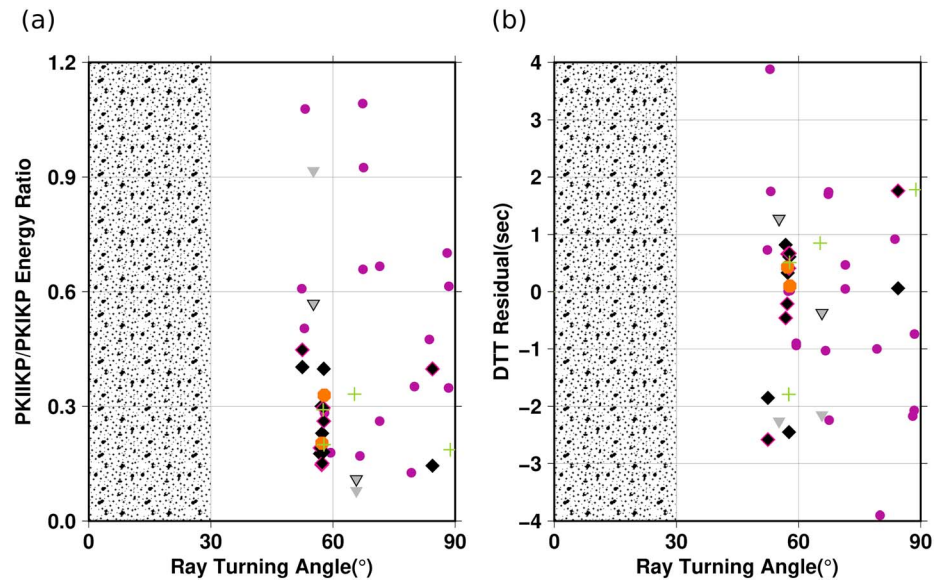
Figure 6. (a) PKIIKP/PKIKP energy ratio and (b) differential travel time residuals (right) with respect to the ray turning angle. Differential travel time residuals are calculated by differencing observed and predicted differential travel times ($T_{PKIIKP} - T_{PKIKP}$). The shaded region indicates where presence of inner core anisotropy is observed. None of our measurements falls within this region. Also, no discernible pattern is present with ray turning angle in either of the measurements, suggesting the effects of anisotropy on measurements are negligible. The meaning of symbols is same as in Figure 4.

are mapped onto the PKIIKP reflection point along the minor arc in Figure 7 for clarity, while they might as well be mapped on to the major arc reflection point. We are unable to separate the amplitude contribution of each PKIIKP ray leg to the total PKIIKP/PKIKP energy ratio when they interfere with each other. Based on the distribution of interference-free major and minor arc PKIIKP/PKIKP ratios (see Figure 6), it could be inferred that total observed PKIIKP energy is equipartitioned between minor and major PKIIKP phases when they interfere. Thus, if the two PKIIKP phases interfere constructively, the energy ratio could reach a value of ~1, consistent with our observations.

Perhaps the most interesting feature in the geographic distribution of energy ratios is the short length-scale nature of variations. The best example of this is observed when considering minor and major arc PKIIKP energy ratios free of any interference (Figure 7). On one hand, a majority of the minor arc PKIIKP reflection points of these data points are located in the Central Pacific region, and their energy ratios vary between ~0.1 and ~0.5 within 10° in latitude (i.e., <200-km along the ICB). Similarly, a majority of energy ratios with major arc PKIIKP reflection points located in Central Africa varies between ~0.1 and ~0.5 within the same lateral distance range as the minor arc data points. The short length scale of the spatial coherence of lateral heterogeneities we thus predict from our data set is consistent with observations of precritical PKiKP amplitudes and waveforms in previous investigations (Krasnoshchekov et al., 2005; Waszek & Deuss, 2015; Tian & Wen, 2017).

5. Discussion

5.1. Links to Previous Observations and Predictions

All five reports of detection of shear waves (PKJKP) in the inner core (Cao & Romanowicz, 2009; Deuss et al., 2000; Julian et al., 1972; Okal & Cansi, 1998; Wookey & Helffrich, 2008), which would provide unequivocal evidence of its solidity, remain controversial (Creager, 2008; Shearer et al., 2011). Nonetheless, based on observations of the PKJKP phase, Wookey and Helffrich (2008) predict that the P wave velocity (V_p) jump across the ICB should be lower than in standard Earth models by as much as 0.40 km/s. In addition, a lower bound for V_s of 2.0 km/s at the top of the inner core is predicted by modeling PKiKP/PcP amplitude ratios (Cao & Romanowicz, 2004; Koper & Dombrovskaya, 2005). Given that these V_s estimates obtained from PKiKP/PcP

(a)

(b)
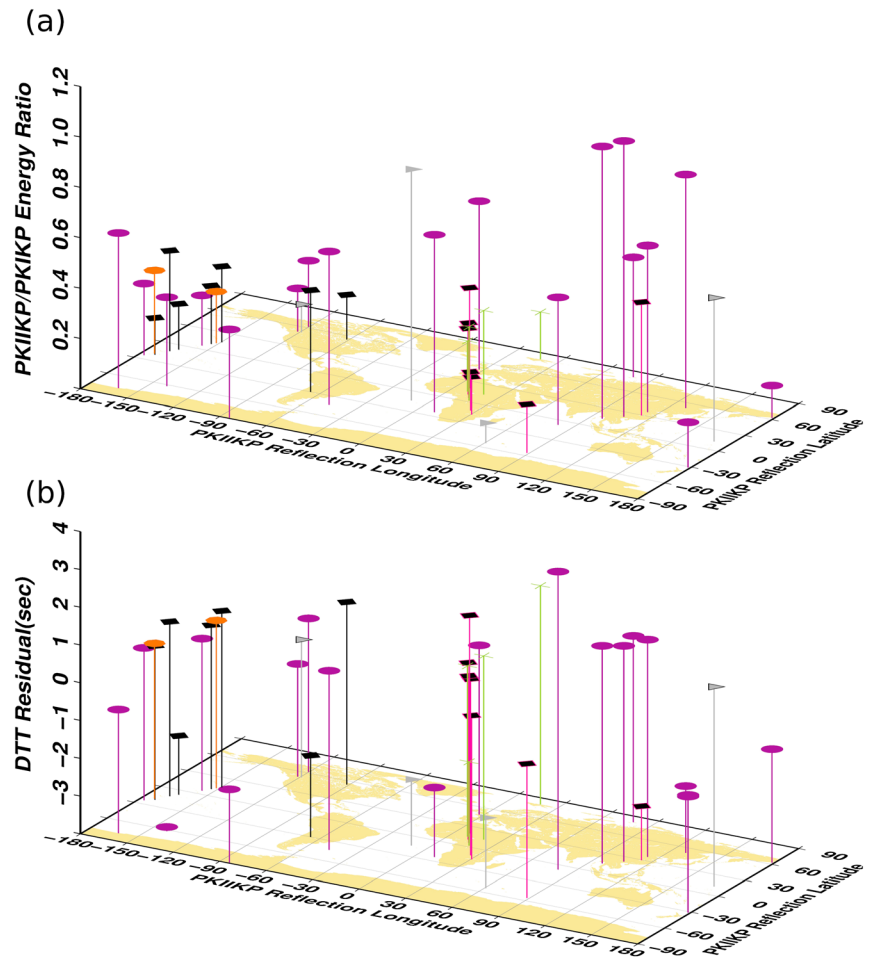
Figure 7. Geographical distribution of (a) PKIIKP/PKIKP energy ratio and (b) PKIIKP-PKIKP differential travel time residuals mapped on to PKIIKP reflection point at the ICB. Data points (purple stems with circular heads) are mapped onto the reflection point along the minor arc of PKIIKP phase when the minor and major arc PKIIKP phases interfere, but they may as well be mapped on to the major arc reflection point. The readers should refer section 4 in the main text for an accurate interpretation. The meaning of stem heads is same as in Figure 4.

ratios and waveforms of PKIKP and PKiKP phases trade off with the P wave quality factor and the density contrast across the ICB (Q_α, Cummins & Johnson, 1988a; Shearer & Masters, 1990; Souriau & Souriau, 1989), the V_s jump across the ICB remains appreciably uncertain. Interestingly, an estimated apparent Q_α as low as 75 for the region immediately below the ICB indicates remarkably high attenuation for a solid medium (Deguen, 2012; Garcia et al., 2004). High attenuation complements predictions of lower V_s (a softer medium) in the uppermost inner core, which can be explained considering dynamics of solidification (Loper & Fearn, 1983; Singh et al., 2000).

Krasnoshchekov et al. (2005) presented evidence supporting an irregular transition at the ICB by modeling absolute amplitudes of precritical PKiKP waves. They proposed a model of *mosaic* ICB structure, in which regions having a liquid-liquid transition are interspersed with those having a liquid-solid transition. Lateral variations observed in PKiKP/PcP amplitude ratios and PKiKP-PcP travel times, as well as complexity observed in precritical PKiKP waveforms, might also support the presence of such a complex ICB structure (Tian & Wen, 2017; Waszek & Deuss, 2015). Seismic and thermodynamic modeling constrains the thickness of transition patches as described by Krasnoshchekov et al. (2005) to less than 10 km (Cummins & Johnson, 1988b; Deguen et al., 2007; Tian & Wen, 2017). Testing this hypothesis is important because geodynamic behavior of a mosaic ICB would be quite different from a uniform ICB with a simple liquid-solid transition.

The hypothesis of an irregular transition layer can be tested by modeling PKIIKP waves at antipodal distances, where their amplitudes are optimum. From a limited data set, Butler and Tsuboi (2010) observed anomalously high PKIIKP amplitudes recorded at these distances. They attribute the origin of this amplitude anomaly mainly to increased impedance contrast at the ICB produced by a sharp ~15% drop in V_p in the bottommost 50 km of the outer core. This model, however, is similar to an original model of Jeffreys (1939) that was used to explain precursors to PKIKP at distances around 130° that were later explained by scattering near the core-mantle boundary in combination with diffraction from the core caustic (Cleary & Haddon, 1972; King et al., 1974). Explaining any regionally varying sharp structures in the liquid outer core is challenging because the low viscosity of the outer core (de Wijs et al., 1998) in combination with vigorous convection predicted in geodynamic models (Calkins et al., 2012) would act to eliminate such structures. In fact, recent velocity models of the bottommost outer core do not support sharp variations in the bottommost outer core (Adam et al., 2018; Souriau, 2015). It is, therefore, reasonable to assume that the observed variations in PKII KP/PKIKP energy ratios originate due to inner core structure rather than sharp velocity gradients in the bottommost outer core.

Our PKIIKP/PKIKP energy ratios deviate from those predicted for the ak135 model. This observation might be either due to a reduction in PKIKP amplitudes, an increase in PKIIKP amplitudes, or both. A significant effect on PKIKP amplitudes due to known inner core structure is not expected unless PKIKP rays propagate quasi-parallel to the Earth's rotation axis (ray turning angle <30°), in which direction attenuation has been observed to be up to 5 times stronger than in the equatorial plane (Souriau & Romanowicz, 1996; Yu & Wen, 2006a). None of our data sample this particular raypath direction in the inner core. Also, the effects of differential attenuation observed in the equatorial plane within the hemispherical structure (Attanayake et al., 2014; Yu & Wen, 2006b) on PKIKP waves are likely to average out at antipodal distances because the PKIKP ray leg in each hemisphere is nearly the same given our source-receiver combinations. This should produce relatively uniform PKIKP amplitudes rather than those varying at much shorter scales as observed here. In addition, the absence of a systematic variation in PKIIKP/PKIKP energy ratios with ray turning angle implies that the amplitude of PKIKP wave is not significantly affected by anisotropy in the inner core. Perhaps inner core anisotropy is not strong enough to produce discernible effects at antipodal distances (Frost & Romanowicz, 2017). On the other hand, PKIIKP waves bottom in the uppermost 80 km of the inner core and thus are unlikely to be affected by anisotropy because the uppermost 100 km of the inner core is generally observed to be isotropic (Irving & Deuss, 2011; Song & Helmberger, 1995). Our energy ratio measurement procedure included the effects of energy redistribution taking place within the PKIKP or PKIIKP pulse due to intrinsic attenuation (Li & Cormier, 2002), scattering (Cormier & Li, 2002), and wave interaction with inner core discontinuities (Song & Helmberger, 1998) accurately, eliminating the amplitude fluctuations from these effects present when amplitude is measured at a single time point (peak or trough).

The region just below the ICB, from where PKIIKP waves is reflected, is likely to have a higher degree of small-scale structural heterogeneity than regions at greater depth in the inner core (Koper et al., 2004; Leyton & Koper, 2007). Recent geodynamic experiments investigating the coupling between core-mantle boundary structure and outer core convection predict that heat extraction near the inner core boundary is heterogeneous at lateral scales as small as hundreds of kilometers (Calkins et al., 2012). Even a small thermal variation near the ICB can result in a large variation in heat extraction (Jones, 2000), whereby growth rate and structure can significantly be affected (Aubert et al., 2008; Gubbins et al., 2011). The spatial scale of dominantly columnar modes of convection in the outer core, tangent to or emanating from the ICB (Maffei et al., 2017), may also affect small-scale structure near the ICB. In combination with the premelting effect (Martorell et al., 2013), we believe that short-scale thermal perturbations accentuate structural heterogeneity just below the ICB and primarily produce strong lateral variations in the shear modulus. Previous lower estimates of shear velocity near the ICB (Cao & Romanowicz, 2004; Koper & Dombrovskaya, 2005; Wookey & Helffrich, 2008) and the prediction of transition patches (e.g., Krasnoshchekov et al., 2005; Tian & Wen, 2017) are consistent with such a dynamic process. In our case, this heterogeneous near-ICB structural model could explain short-scale PKIIKP/PKIKP energy ratios because PKIIKP reflectivity is strongly sensitive to shear modulus at the ICB (Cormier, 2015; Cormier et al., 2011). To test this hypothesis, we conducted a preliminary model space exploration, where we determine the nature of a transition layer with a reduced shear modulus required to generate the observed distribution of PKIIKP/PKIKP energy ratios.
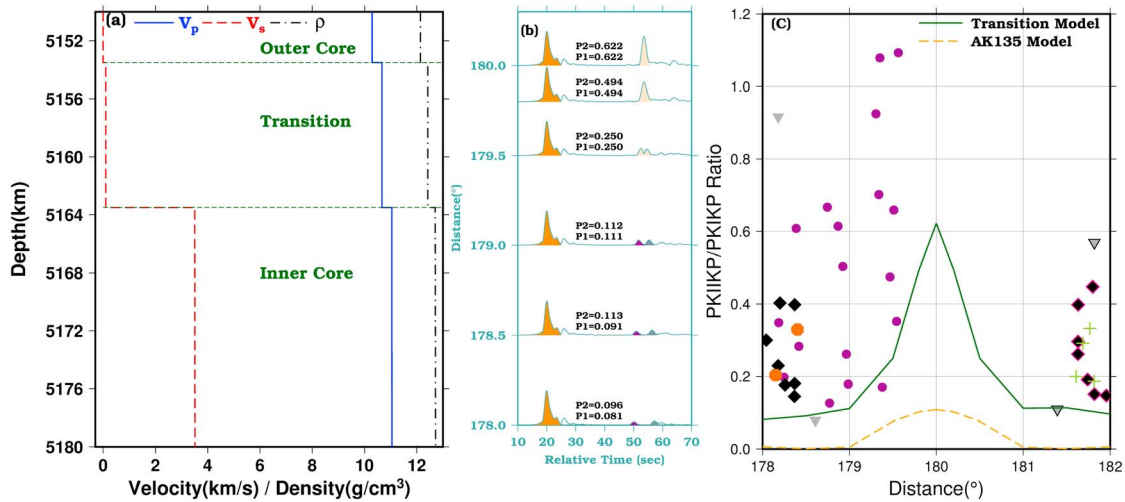
Figure 8. Synthetics with an explosion source. (a) The model for generating higher energy ratios illustrated by the green curve in (c). (b) Energy envelopes predicted for the model shown in (a). P1 and P2 are energy ratios for minor and major arc waveforms, respectively. Energy pulses are PKIKP (orange), minor arc PKIIKP (purple), and major arc PKIIKP (gray). When minor and major arc PKIIKP interfere, the pulses are colored beige. (c) Energy ratios as a function of distance. Predictions for the model in (a) and those for the ak135 model are shown with a green solid line and orange dashed line, respectively. Also shown are observations. Symbols are the same as in Figure 4.
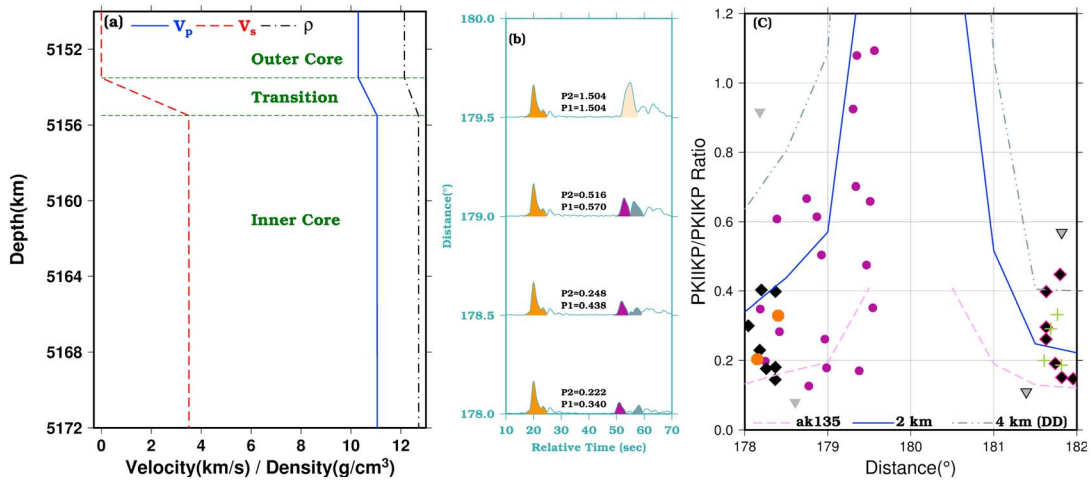
5.2. Preliminary Model Space Exploration

We compute full waveform synthetics accurate up to 1 Hz in the 178°–180° distance range using the direct solution method (Geller & Takeuchi, 1995; Kawai et al., 2006) with a 600-km deep explosion source and process them as we did with our data to obtain synthetic PKIIKP/PKIKP energy ratios. We test both gradient models of V_p, V_s, and density as well as discontinuity models (e.g., Tian & Wen, 2017) using ak135 model as the reference. In each of our tests, we hold constant the inner core shear quality factor at 85 ($Q\mu$) and use a depth-varying bulk quality factor ($Q\kappa$), where it is 269.5 in the transition layer, 358.5 in the uppermost 100 km excluding the transition layer, and 610 in the rest of the inner core. The estimates of $Q\kappa$ for the transition and the uppermost 100 km are obtained using the equations given by Anderson and Hart (1978) and compressional attenuation (Q_α) estimated by Attanayake et al. (2014) from full waveform inversion. $Q\kappa$ in the rest of the layers of the Earth model is set to those given in the ak135 reference model. Our parameter range is as follows: transitional layer thickness is 0–20 km (increment of 1 km), V_p is 10.2890–11.0427 km/s (increment [10.2890–11.0427] × 10%), V_s is 0.1–3.5 km/s (increment 0.2 km/s), and density is 12139–12,704 kg/m^3 (increment [12,139–12,704] × 10%). We vary these parameters to generate physically plausible models and predict PKIIKP/PKIKP energy ratios. A key constrain we have in our observations is the gradual increase in PKIIKP/PKIKP energy ratio envelope from ~0.4 at ~178° to a maximum of ~1.1 at ~179.5°, and we attempted to match this trend with our synthetics.

We find that the steep energy ratio envelope observed in our data cannot be reproduced with an explosion source. The best fitting model we obtained has a transition characterized by uniform V_p, V_s, and density with a thickness of 10 km, where V_s = 0.1, and V_p and density jumps at the ICB is ~50% of that found in the reference ak135 model (Figure 8a). This model is similar to the one proposed by Tian and Wen (2017) for predicting precritical PKiKP waveforms except that we place constrains on the V_s structure. Setting V_s = 0 and/or increasing the V_p and density jump (e.g., Cormier, 2015) produces a steeper energy ratio envelope, but we exclude this choice because there is no physical interpretation for such a model. In Figure 8b we show predictions of energy envelopes based on this particular model, and in Figure 8c we show predictions and observations of energy ratios as a function of distance. It is clear that predicted ratios are underpredicted and they do not approach the observed maximum value of ~1.1 even at 180°, where energy from all azimuths converges.

5.2.1. Effect of Radiation Pattern on Structure

We conducted tests by including the effect of radiation pattern on predicted energy ratios for events in our data set. This was achieved by synthesizing seismograms with moment tensor solutions given in the GCMT catalogue (Ekström et al., 2012). We find that the radiation pattern affects energy ratios, for which a

AGU
100
ADVANCING EARTH
AND SPACE SCIENCE

Geochemistry, Geophysics, Geosystems

10.1029/2018GC007562

Figure 9. Same as Figure (8) but for a source modeled with moment tensor solution given in the GCMT catalogue for the 21 March 2005 M = 6.4 earthquake in Argentina. The energy envelope (c) is predicted with a gradient model of transition (a) whose thickness is 2 km. Predictions for a 4-km-thick double discontinuity model is also shown in (c). See also supporting information Figure S4.

representative example is given in Figure 9. This demonstrates that a better fit between the observed data and the predicted envelope can be achieved when the radiation pattern is taken into account in combination with a model of the transition layer. For any given event and its corresponding radiation pattern, we observe consistently across all events that the predictions based on the ak135 model are only producing a lower bound to the energy ratios, which warrants the inclusion of an irregular transition structure at the ICB to fit the observed energy ratio envelope. In the example case in Figure 9, the velocity and density profiles of the transition layer are described by gradients without having additional discontinuities, where the minimum required thickness of the transition layer is about 2 km. Also shown in Figure 9c are predictions for a double discontinuity model, where the second discontinuity is located 4 km below the ICB (see supporting information Figure S4).

5.3. Transition Models: Main Features and Implications to Dynamics

No single model of a transition layer explains all our data, implying that the characteristics of the transition must be spatially varying. An irregular transition (a *patchy* inner core boundary) whose characteristics vary, as inferred here, appears to favor nonlinear solidification models, where inner core growth is locally modulated by thermal perturbations at the ICB (Bergman et al., 1999; Bergman & Fearn, 1994; Calkins et al., 2012; Ren et al., 2016; Yu et al., 2015). Based on our observations, the hypothesis of isothermal, and therefore, uniform growth leading to an inner core void of a mushy region can be rejected (Morse, 2002).

Our preliminary numerical tests provide first order constrains on finiteness of the thickness of a liquid-to-solid transitional layer. Because the ak135 model produces a minimum bound to energy ratios, it can be inferred that the minimum thickness of the transitional layer is 0 km along the ICB. Note that we are unable to differentiate a sharp discontinuity from a thin transitional layer with a thickness of a couple of hundred meters because our data are not sensitive to such thin layers. We find that the maximum thickness of a transition need not exceed 10 km to fit our data envelope. This estimate agrees with analytical predictions of Phinney (1970) for high-frequency waves, and that based on high-frequency precritical PKiKP and PKIKP waveforms (Cummins & Johnson, 1988b; Kawakatsu, 2006; Koper & Dombrovskaya, 2005; Souriau & Souriau, 1989; Tian & Wen, 2017). Broad radial averaging associated with normal modes would prevent resolving this complexity at the top of the inner core. Thus, ours is an important constraint to be considered in dynamic modeling, where the thickness of the transition layer remains unconstrained (e.g., Deguen et al., 2007).

When the radiation pattern is taken into account, gradient models are preferred over models having an additional discontinuity in the uppermost 10 km of the inner core. This prediction is consistent with geodynamic analogue experiments that show a gradual increase in solid fraction on the solid side of the liquid-solid

interface (Spetzler & Anderson, 1968; Yu et al., 2015). Models having an additional discontinuity, however, can explain anomalously high spatially localized PKIIKP/PKIKP energy ratios if the velocity and density profiles are uniform (i.e., no gradient) between the ICB and the additional discontinuity (e.g., see Figures 9c and S4). We find that these models have a lower V_s value within the transition (~2–3 km/s). We observe anomalously high major arc energy ratios (and the single noninterfering minor arc measurement of ~0.9) from waves sampling a region beneath Africa (Figures 5 and 7). Our data suggest that this is a candidate region for locating an additional discontinuity in the upper 10 km of the inner core. Alternatively, complex 3-D wave propagation effects that we do not capture in our 1-D simulations could produce these anomalous energy ratios. Note that this region is characterized by shallow anisotropy (Yu & Wen, 2007), located adjacent to a region that appears to be growing faster (Cormier & Attanayake, 2013), and broadly marks the transition between the quasi-Eastern and quasi-Western Hemispheres in the upper inner core (Waszek et al., 2011).

5.4. Coda Waves

Hybrid models with an additional discontinuity in the uppermost 10 km below the ICB and a gradient in velocities and density between the two discontinuities produce PKIKP coda waves both at shorter (130°–140°) and antipodal distances (supporting information Figure S5) if $V_s < 2$ km/s and the additional V_p discontinuity is ~50% that of the ak135 model. Small-scale volumetric heterogeneities in the uppermost 300 km of the inner core are considered as the origin of seismic coda waves (Koper et al., 2004; Leyton & Koper, 2007; Vidale & Earle, 2000). Our tests, however, suggest that energy trapped in a transition layer can also contribute to seismic coda, particularly within a narrow time window of inner core-sampling phase arrivals.

5.5. Other Effects and Future Computations

The effect of inner core ellipticity, crustal and mantle structure, and ICB topography on our data should also be considered. Our initial analyses suggest that they do not affect our measurements significantly, and we discuss these factors in detail in supporting information (Bolt, 1977; Bolt & O'Neill, 1965; Butler, 1986; Cao et al., 2007; Dai et al., 2012; de Silva et al., 2017; Iritani et al., 2014; Kennett & Gudmundsson, 1996; Koot & Dumberry, 2011; McNamara et al., 2010; Ohtaki et al., 2012; Pejić et al., 2017; Shen et al., 2016; Tkalčić et al., 2010; Wen & Niu, 2002; Zheng & Wu, 2008). The computational methods available at present are not adequate to compute high-frequency (up to 1 Hz) waves at antipodal distances in 3-D realistic media, which is important given the emerging complex structure of the inner core (Tkalčić, 2015). When such methods become more computationally feasible, 3-D effects of these external factors can also be tested numerically.

6. Conclusions

We processed a unique data set of PKIKP and PKIIKP waveforms recorded near the antipode of earthquakes. Both array processing and individual waveform analyses were used to investigate PKIIKP/PKIKP energy ratios. The array processing was not successful at detecting PKIIKP.

waveforms for four specific reasons: (1) central stations were too far out from the antipode, eliminating PKIIKP detection due to reduced amplitudes; (2) PKIKP signal-generated coda masks the PKIIKP arrival time window; (3) plane wave approximation needed in our array processing method breaks down closer to the antipode; and (4) possible interaction of high frequency waves with small scale heterogeneity. Forty-two energy ratios measured from 33 envelopes of individual velocity seismograms show significant variation, ranging from ~0.1 to ~1.1, and along with differential travel time residuals, they do not show a discernible spatial pattern with the ray turning angle, suggesting that inner core anisotropy is not the origin of observed short-scale variability. This implies that reflectivity properties of PKIIKP phase must be changing along the inner core boundary. The variability of our energy ratios cannot be explained by a simple uniform inner core boundary as predicted in standard Earth models. In fact, our results are consistent with the presence of an irregular transition layer below the inner core boundary whose characteristics are spatially varying. Our preliminary model exploration suggests that the transition layer is likely characterized by a steep gradient (V_p, V_s, and density) with a variable thickness of 0 to 10 km, and in some localized regions a double discontinuity in the uppermost 10 km of the inner core. The energy trapped in such a transition layer can also contribute to coda waves if V_s is smaller than about 2 km/s. Fine-scale structural features of this nature are important for understanding the geodynamics of inner core growth. The most plausible explanation for the presence of an irregular transition layer having variable rigidity is nonlinear solidification driven by small-scale

convection in the bottommost outer core that produces short-scale thermal perturbations along the inner core boundary (e.g., Calkins et al., 2012; Yu et al., 2015).

References

Adam, J. M.-C., Ibourichène, A., & Romanowicz, B. (2018). Observation of core sensitive phases: Constraints on the velocity and attenuation profile in the vicinity of the inner-core boundary. *Physics of the Earth and Planetary Interiors*, *275*, 19–31. https://doi.org/10.1016/j.pepi.2017.12.008

Alboussière, T., Deguen, R., & Melzani, M. (2010). Melting-induced stratification above the Earth's inner core due to convective translation. *Nature*, *466*(7307), 744–747. https://doi.org/10.1038/nature09257

Anderson, D. L., & Hart, R. S. (1978). Attenuation models of the earth. *Physics of the Earth and Planetary Interiors*, *16*(4), 289–306. https://doi.org/10.1016/0031-9201(78)90068-7

Anderson, O. L., & Isaak, D. G. (2002). Another look at the core density deficit of Earth's outer core. *Physics of the Earth and Planetary Interiors*, *131*, 19–27.

Attanayake, J., Cormier, V. F., & deSilva, S. M. (2014). Uppermost inner core seismic structure—New insights from body waveform inversion. *Earth and Planetary Science Letters*, *385*, 49–58.

Aubert, J., Amit, H., Hulot, G., & Olson, P. (2008). Thermochemical flows couple the Earth's inner core growth to mantle heterogeneity. *Nature*, *454*, 758–761.

Bergman, M. I., & Fearn, D. R. (1994). Chimneys on the inner core boundary? *Geophysical Research Letters*, *21*(6), 477–480.

Bergman, M. I., Fearn, D. R., & Bloxham, J. (1999). Suppression of channel convection in alloys via an applied magnetic field. *Journal of Metallurgical and Materials Transactions A*, *30*, 1809–1815. https://doi.org/10.1007/s11661-999-0179-5

Bolt, B. A. (1977). The detection of PKIIKP and damping in the inner core. *Annali di Geofisica*, *30*, 507–520.

Bolt, B. A., & O'Neill, M. E. (1965). *Geophysical Journal of the Royal Astronomical Society*, *9*, 223–231.

Butler, R. (1986). Amplitudes at the antipode. *Bulletin of the Seismological Society of America*, *76*(6), 1355–1365.

Butler, R., & Tsuboi, S. (2010). Antipodal seismic observations of temporal and global variation at Earth's inner-outer core boundary. *Geophysical Research Letters*, *37*, L11301. https://doi.org/10.1029/2010GL042908

Calkins, M. A., Noir, J., Eldredge, J. D., & Aurnou, J. M. (2012). The effects of boundary topography on convection in Earth's core. *Geophysical Journal International*, *189*, 799–814. https://doi.org/10.1111/j.1365-246X.2012.05415.x

Cao, A., Masson, Y., & Romanowicz, B. (2007). Short wavelength topography on the inner-core boundary. *Proceedings of the National Academy of Sciences of the United States of America*, *104*(1), 31–35. https://doi.org/10.1073/pnas.0609810104

Cao, A., & Romanowicz, B. (2004). Constraints on density and shear velocity contrasts at the inner core boundary. *Geophysical Journal International*, *157*, 1146–1151. https://doi.org/10.1111/j.1365-246X.2004.02330.x

Cao, A., & Romanowicz, B. (2009). Constraints on shear wave attenuation in the Earth's inner core from an observation of PKJKP. *Geophysical Research Letters*, *36*, L09301. https://doi.org/10.1029/2009GL038342

Červeny, V. (2001). *Seismic ray theory*. Cambridge: Cambridge University Press.

Chen, B., Li, Z., Zhang, D., Liu, J., Hu, M. Y., Zhao, J., et al. (2014). Hidden carbon in Earth's inner core revealed by shear softening in dense Fe_7C_3. *Proceedings of the National Academy of Sciences of the United States of America*, *111*(50), 17,755–17,758. https://doi.org/10.1073/pnas.1411154111

Cleary, J. R., & Haddon, R. A. W. (1972). Seismic wave scattering near the core-mantle boundary: A new interpretation of precursors to PKP. *Nature*, *240*, 549–551.

Cormier, V. F. (2015). Detection of inner core solidification from observations of antipodal PKIIKP. *Geophysical Research Letters*, *42*, 7459–7466. https://doi.org/10.1002/2015GL065367

Cormier, V. F., & Attanayake, J. (2013). Earth's solid inner core: Seismic implications of freezing and melting. *Journal of Earth Science*, *24*(5). https://doi.org/10.1007/s12583-013-0363-9

Cormier, V. F., Attanayake, J., & He, K. (2011). Inner core freezing and melting: Constraints from seismic body waves. *Physics of the Earth and Planetary Interiors*, *188*(3–4), 163–172. https://doi.org/10.1016/j.pepi.2011.07.007

Cormier, V. F., & Li, X. (2002). Frequency-dependent seismic attenuation in the inner core, 2, A scattering and fabric interpretation. *Journal of Geophysical Research*, *107*(B12), 2362. https://doi.org/10.1029/2002JB001796

Cottaar, S., & Buffett, B. (2012). Convection in the Earth's inner core. *Physics of the Earth and Planetary Interiors*, *198–199*, 67–78. https://doi.org/10.1016/j.pepi.2012.03.008

Creager, K. C. (2008). Solid evidence in the inner core. *Nature*, *454*, 833–834.

Crotwell, H. P., Owens, T. J., & Ritsema, J. (1999). The TauP ToolKit: Flexible seismic travel-time and raypath utilities. *Seismological Research Letters*, *70*(2), 154–160. https://doi.org/10.1785/gssrl.70.2.154

Cummins, P., & Johnson, L. R. (1988a). Short-period body wave constraints of properties of the Earth's inner core boundary. *Journal of Geophysical Research*, *93*, 9058–9074. https://doi.org/10.1029/JB093iB08p09058

Cummins, P., & Johnson, L. R. (1988b). Synthetic seismograms for an inner core transition of finite thickness. *Geophysical Journal*, *94*, 21–34.

Dai, Z., Wang, W., & Wen, L. (2012). Irregular topography at the Earth's inner core boundary. *Proceedings of the National Academy of Sciences of the United States of America*, *109*(20), 7654–7658. https://doi.org/10.1073/pnas.1116342109

Das, T., Chatterjee, S., Ghosh, S., & Saha-Dasgupta, T. (2017). First-principles prediction of Si-doped Fe carbide as one of the possible constituents of Earth's inner core. *Geophysical Research Letters*, *44*, 8776–8784. https://doi.org/10.1002/2017GL073545

Deguen, R. (2012). Structure and dynamics of Earth's inner core. *Earth and Planetary Science Letters*, *333–334*, 211–225. https://doi.org/10.1016/j.epsl.2012.04.038

Deguen, R., Alboussière, T., & Brito, D. (2007). On the presence and structure of a mush at the inner core boundary of the Earth. *Physics of the Earth and Planetary Interiors*, *274*, 1887–1891.

Deuss, A., Woodhouse, J. H., Paulssen, H., & Trampert, J. (2000). The observation of inner core shear waves. *Geophysical Journal International*, *142*, 67–73.

de Silva, S., Cormier, V. F., & Zheng, Y. (2017). Inner core boundary topography explored with reflected and diffracted P waves. *Physics of the Earth and Planetary Interiors*. https://doi.org/10.1016/j.pepi.2017.04.008

de Wijs, G., Kresse, G., Vočadlo, L., Dobson, D., Alf, D., Gillan, M., & Price, G. (1998). The viscosity of liquid iron under Earth's core conditions. *Nature*, *392*, 805–807.

Dziewonski, A. (1971). Overtones of free oscillations and the structure of the Earth's interior. *Science*, *172*, 1336–1338.

Ekström, G., Nettles, M., & Dziewonski, A. M. (2012). The global CMT project 2004–2010: Centroid-moment tensors for 13,017 earthquakes. *Physics of the Earth and Planetary Interiors*, *200–201*, 1–9. https://doi.org/10.1016/j.pepi.2012.04.002

Frost, D., & Romanowicz, B. (2017). Constraints on inner core anisotropy using array observations of P′P′. *Geophysical Research Letters*, *44*, 10,878–10,886. https://doi.org/10.1002/2017GL075049

Garcia, R., Chevrot, S., & Weber, M. (2004). Nonlinear waveform and delay time analysis of triplicated core phases. *Journal of Geophysical Research*, *109*, B01306. https://doi.org/10.1029/2003JB002429

Geller, R. J., & Takeuchi, N. (1995). A new method for computing highly accurate DSM synthetic seismograms. *Geophysical Journal International*, *123*, 449–470.

Gleason, A. E., & Mao, W. L. (2013). Strength of iron at core pressures and evidence for a weak Earth's inner core. *Nature Geoscience*, *6*(7), 571–574. https://doi.org/10.1038/ngeo1808

Goldstein, P., Dodge, D., Firpo, M., & Minner, L. (2003). SAC2000: Signal processing and analysis tools for seismologists and engineers. In W. H. K. Lee, H. Kanamori, P. C. Jennings, & C. Kisslinger (Eds.), *Invited contribution to The IASPEI International Handbook of Earthquake and Engineering Seismology*. London: Academic Press.

Gubbins, D., Alfè, D., & Davies, C. J. (2013). Compositional instability of Earth's solid inner core. *Geophysical Research Letters*, *40*, 1084–1088. https://doi.org/10.1002/grl.50186

Gubbins, D., Sreenivasan, B., Mound, J., & Rost, S. (2011). Melting of the Earth's inner core. *Nature*, *473*, 361–364.

Iritani, R., Takeuchi, N., & Kawakatsu, H. (2014). Intricate heterogeneous structures of the top 300 km of the Earth's inner core inferred from global array data: II. Frequency dependence of inner core attenuation and its implication. *Earth and Planetary Science Letters*, *405*, 231–243. https://doi.org/10.1016/j.epsl.2014.08.038

Irving, J. C. E., & Deuss, A. (2011). Stratified anisotropic structure at the top of Earth's inner core: A normal mode study. *Physics of the Earth and Planetary Interiors*, *186*, 59–69. https://doi.org/10.1016/j.pepi.2011.03.003

Jeffreys, H. (1939). The times of the core waves, M.N.R.A.S. *Geophysical Supplement*, *4*, 548–561.

Jones, C. A. (2000). Convection-driven geodynamo models. *Philosophical Transactions of the Royal Society of London*, *358*, 873–897.

Julian, B. R., Davies, D., & Sheppard, R. M. (1972). PKJKP. *Nature*, *235*, 317–318.

Kawai, K., Takeuchi, N., & Geller, R. J. (2006). Complete synthetic seismograms up to 2 Hz for transversely isotropic spherically symmetric media. *Geophysical Journal International*, *164*, 411–424. https://doi.org/10.1111/j.1365-246X.2005.02829.x

Kawakatsu, H. (2006). Sharp and seismically transparent inner core boundary region revealed by an entire network observation of near vertical PKiKP. *Earth, Planets and Space*, *58*, 855–863.

Kennett, B. L. N., & Gudmundsson, O. (1996). Ellipticity corrections for seismic phases. *Geophysical Journal International*, *127*, 40–48.

King, D. W., Haddon, R. A., & Cleary, J. R. (1974). Array analysis of precursors to *PKIKP* in the distance range 128° to 142°. *Geophysical Journal of the Royal Astronomical Society*, *37*, 157–173. https://doi.org/10.1111/j.1365-246X.1974.tb02450.x

Koot, L., & Dumberry, M. (2011). Viscosity of the Earth's inner core: Constraints from nutation observations. *Earth and Planetary Science Letters*, *308*, 343–349. https://doi.org/10.1016/j.epsl.2011.06.004

Koper, K. D., & Dombrovskaya, M. (2005). Seismic properties of the inner core boundary from PKiKP/P amplitude ratios. *Earth and Planetary Science Letters*, *237*, 680–694.

Koper, K. D., Franks, J. M., & Dombrovskaya, M. (2004). Evidence for small-scale heterogeneity in Earth's inner core from a global study of PKiKP coda waves. *Earth and Planetary Science Letters*, *228*, 227–241.

Koper, K. D., Pyle, M. L., & Franks, J. M. (2003). Constraints on aspherical core structure from PKiKP-PcP differential travel times. *Journal of Geophysical Research*, *108*(B3), 2168. https://doi.org/10.1029/2002JB001995

Krasnoshchekov, D. N., Kazik, P. B., & Ovtchinnikov, V. M. (2005). Seismological evidence for mosaic structure of the surface of the Earth's inner core. *Nature*, *435*, 483–487.

Kvasnička, M., & Jansky, J. (1999). Fresnel volumes corresponding to PKP waves in the IASP91 model. *Journal of Seismology*, *3*, 375–391.

Leyton, F., & Koper, K. D. (2007). Using PKiKP coda to determine inner core structure: 2. Determination of QC. *Journal of Geophysical Research*, *112*, B05317. https://doi.org/10.1029/2006JB004370

Li, X., & Cormier, V. F. (2002). Frequency-dependent seismic attenuation in the inner core, 1, A viscoelastic interpretation. *Journal of Geophysical Research*, *107*(B12), 2361. https://doi.org/10.1029/2002JB001795

Li, Y., Vočadlo, L., Brodholt, J., & Wood, I. G. (2016). Thermoelasticity of Fe_7C_3 under inner core conditions. *Journal of Geophysical Research: Solid Earth*, *121*, 5828–5837. https://doi.org/10.1002/2016JB013155

Loper, D. E., & Fearn, D. R. (1983). A seismic model of a partially molten inner core. *Journal of Geophysical Research*, *88*, 1235–1242.

Maffei, S., Jackson, A., & Livermore, P. W. (2017). Characterization of columnar intertial modes in rapidly rotating spheres and spheroids. *Proceedings of the Royal Society A*, *473*, 20170181. https://doi.org/10.101098/rspa.2018.0181

Martorell, B., Vočadlo, L., Brodholt, J., & Wood, I. G. (2013). Strong pre-melting effect in the elastic properties of hcp-Fe under inner-core conditions. *Science*, *342*, 466–468.

Martorell, B., Wood, I. G., Brodholt, J., & Vočadlo, L. (2016). The elastic properties of hcp-FeSi at Earth's inner-core conditions. *Earth and Planetary Science Letters*, *451*, 89–96. https://doi.org/10.1016/j.epsl.2016.07.018

McFadden, P. L., Drummond, B. J., & Kravis, S. (1986). The *N*th-root stack: Theory, applications, and examples. *Geophysics*, *51*, 1879–1892.

McNamara, A. K., Garnero, E. J., & Rost, S. (2010). Tracking deep mantle reservoirs with ultra-low velocity zones. *Earth and Planetary Science Letters*, *299*, 1–9. https://doi.org/10.1016/j.epsl.2010.07.042

Miller, M. S., Niu, F., & Vanacore, E. A. (2013). Aspherical structural heterogeneity within the uppermost inner core: insights into the hemispherical boundaries and core formation. *Physics of the Earth and Planetary Interiors*, *223*, 8–20. https://doi.org/10.1016/j.pepi.2013.02.001

Monnereau, M., Calvet, M., Margerin, L., & Souriau, A. (2010). Lopsided growth of the earth's inner core. *Science*, *328*, 1014–1017.

Montagner, J.-P., & Kennett, B. L. N. (1996). How to reconcile body-wave and normal-mode reference Earth models. *Geophysical Journal International*, *125*, 229–248. https://doi.org/10.1111/j.1365-246X.1996.tb06548.x

Morse, S. A. (2002). No mushy zones in the Earth's core. *Geochemica et Cosmochemica Acta*, *66*(12), 2155–2165.

Niu, F., & Chen, Q.-F. (2008). Seismic evidence for distinct anisotropy in the innermost inner core. *Nature Geoscience*, *1*, 692–696. https://doi.org/10.1038/ngeo314

Ohtaki, T., Kaneshima, S., & Kanjo, K. (2012). Seismic structure near the inner core boundary in the south polar region. *Journal of Geophysical Research*, *117*, B03312. https://doi.org/10.1029/2011JB008717

Okal, E., & Cansi, Y. (1998). Detection of PKJKP at intermediate periods by progressive multi-channel correlation. *Earth and Planetary Science Letters*, *164*, 23–30.

Owens, T. J., Crotwell, H. P., Groves, C., & Oliver-Paul, P. (2004). SOD: Standing order for data. *Seismological Research Letters*, *75*, 515–520.

Pejić, T., Tkalčić, H., Sambridge, M., Cormier, V. F., & Benavente, R. (2017). Attenuation tomography of the upper inner core. *Journal of Geophysical Research: Solid Earth*, *122*, 3008–3032. https://doi.org/10.1002/2016JB013692

Phinney, R. A. (1970). Reflection of acoustic waves from a continuously varying interfacial region. *Reviews of Geophysics and Space Physics*, *8*, 517–532.

Prescher, C., Dubrovinsky, L., Bykova, E., Kupenko, I., Glazyrin, K., Kantor, A., et al. (2015). High Poisson's ratio of Earth's inner core explained by carbon alloying. *Nature Geoscience*, *8*(3), 220–223. https://doi.org/10.1038/NGEO2370

Ren, W. L., Fan, Y. F., Feng, J. W., Zhong, Y. B., Yu, J. B., Ren, Z. M., & Liaw, P. K. (2016). Non-monotonic changes in critical solidification rates for stability of liquid-solid interfaces with static magnetic fields. *Nature Scientific Reports*, *6*, 20,598. https://doi.org/10.1038/srep20598

Rial, J. A., & Cormier, V. F. (1980). Seismic waves at the epicenter's antipode. *Journal of Geophysical Research*, *85*, 2661–2668. https://doi.org/10.1029/JB085iB05p02661

Romanowicz, B., Cao, A., Godwal, B., Wenk, R., Ventosa, S., & Jeanloz, R. (2016). Seismic anisotropy in the Earth's innermost inner core: Testing structural models against mineral physics predictions. *Geophysical Research Letters*, *43*, 93–100. https://doi.org/10.1002/2015GL066734

Romanowicz, B., Tkalčić, H., & Bréger, L. (2003). On the origin of complexity in PKP travel time data. In V. Dehant, K. C. Creager, S.-I. Karato, & S. Zatman (Eds.), *Earth's Core: Dynamics, Structure, Rotation* (pp. 31–44). Washington, DC: American Geophysical Union.

Rost, S., & Thomas, C. (2002). Array seismology: Methods and application. *Reviews of Geophysics*, *40*(3), 1008. https://doi.org/10.1029/2000RG000100

Rost, S., & Thomas, C. (2009). Improving seismic resolution through array processing techniques. *Surveys in Geophysics*, *30*, 271–299. https://doi.org/10.1007/s10712-009-9070-6

Shearer, P. M., & Masters, G. (1990). The density and shear velocity contrast at the inner core boundary. *Geophysical Journal International*, *102*, 491–498.

Shearer, P. M., Rychert, C. A., & Liu, Q. (2011). On the visibility of the inner-core shear wave phase PKJKP at long periods. *Geophysical Journal International*, *185*, 1379–1383. https://doi.org/10.1111/j.1365-246X.2011.05011.x

Shen, Z., Ai, Y., He, Y., & Jiang, M. (2016). Using pre-critical PKiKP–PcP phases to constrain the regional structures of the inner core boundary beneath East Asia. *Physics of the Earth and Planetary Interiors*, *252*, 37–48. https://doi.org/10.1016/j.pepi.2016.01.001

Singh, S. C., Taylor, M. A. J., & Montagner, J. P. (2000). On the presence of liquid in Earth's inner core. *Science*, *287*, 2471–2474.

Song, X., & Helmberger, D. V. (1995). Depth dependence of anisotropy of Earth's inner core. *Journal of Geophysical Research*, *100*, 9805–9816. https://doi.org/10.1029/95JB00244

Song, X., & Helmberger, D. V. (1998). Seismic evidence for an inner core transition zone. *Science*, *282*, 924–927.

Souriau, A. (2015). Presumption of large-scale heterogeneity at the top of the outer core. *Earth and Planetary Science Letters*, *415*, 175–182. https://doi.org/10.1016/j.epsl.2015.01.024

Souriau, A., & Romanowicz, B. (1996). Anisotropy in inner core attenuation: A new type of data to constrain the nature of the solid core. *Geophysical Research Letters*, *23*, 1–4. https://doi.org/10.1029/95GL03583

Souriau, A., & Souriau, M. (1989). Ellipticity and density at the inner core boundary from subcritical PKiKP and PcP data. *Geophysical Journal International*, *98*, 39–54. https://doi.org/10.1111/j.1365-246X.1989.tb05512.x

Spetzler, H., & Anderson, D. L. (1968). The effect of temperature and partial melting on velocity and attenuation in a simple binary system. *Journal of Geophysical Research*, *73*, 6051–6060. https://doi.org/10.1029/JB073i018p06051

Stammler, K. (1993). Seismic handler: Programmable multi-channel data handler for interactive and automatic processing of seismic analyses. *Computational Geosciences*, *19*(2), 135–140. https://doi.org/10.1016/0098-3004(93)90110-Q

Stroujkova, A., & Cormier, V. F. (2004). Regional variations in the uppermost 100 km of the Earth's inner core. *Journal of Geophysical Research*, *109*, B10307. https://doi.org/10.1029/2004JB002976

Tian, D., & Wen, L. (2017). Seismological evidence for a localized mushy zone at the Earth's inner core boundary. *Nature Communications*, *8*, 165. https://doi.org/10.1038/s41467-017-00229-9

Tkalčić, H. (2015). Complex inner core of the Earth: The last frontier of global seismology. *Reviews of Geophysics*, *53*, 59–94. https://doi.org/10.1002/2014RG000469

Tkalčić, H., Cormier, V. F., & He, K. (2010). Steep reflections from the earth's core reveal small-scale heterogeneity in the upper mantle. *Physics of the Earth and Planetary Interiors*, *178*, 80–91.

Vidale, J. E., & Earle, P. S. (2000). Fine-scale heterogeneity in the Earth's inner core. *Nature*, *404*, 273–275.

Vočadlo, L. (2007). Ab initio calculations of the elasticity of iron alloys at inner core conditions: Evidence for a partially molten inner core? *Earth and Planetary Science Letters*, *254*, 227–232.

Wang, T., Song, X., & Xia, H. H. (2015). Equatorial anisotropy in the inner part of the Earth's inner core from autocorrelation of earthquake coda. *Nature Geoscience*, *8*, 224–227. https://doi.org/10.1038/NGEO2354

Waszek, L., & Deuss, A. (2015). Anomalously strong observations of PKiKP/PcP amplitude ratios on a global scale. *Journal of Geophysical Research: Solid Earth*, *120*, 5175–5190. https://doi.org/10.1002/2015JB012038

Waszek, L., Irving, J., & Deuss, A. (2011). Reconciling the hemispherical structure of Earth's inner core with its super-rotation. *Nature Geoscience*, *4*, 264–267.

Wen, L., & Niu, F. (2002). Seismic velocity and attenuation structures in the top of the Earth's inner core. *Journal of Geophysical Research*, *107*(B11), 2273. https://doi.org/10.1029/2001JB000170

Wessel, P., Smith, W. H. F., Scharroo, R., Luis, J., & Wobbe, F. (2013). Generic Mapping Tools: Improved version released. *Eos, Transactions American Geophysical Union*, *94*(45), 409–410. https://doi.org/10.1002/2013EO450001

Wookey, J., & Helffrich, G. (2008). Inner-core shear-wave anisotropy and texture from an observation of PKJKP waves. *Nature*, *454*, 873–877. https://doi.org/10.1038/nature07131

Yu, J., Bergman, M. I., Huguet, L., & Alboussiere, T. (2015). Partial melting of a Pb-Sn mushy layer due to heating from above, and implications for regional melting of Earth's directionally solidified inner core. *Geophysical Research Letters*, *42*, 7046–7053. https://doi.org/10.1002/2015GL064908

Yu, W.-c., Su, J., Song, T.-R. A., Huang, H.-H., Mozziconacci, L., & Huang, B.-S. (2017). The inner core hemispheric boundary near 180°W. *Physics of the Earth and Planetary Interiors*, *272*, 1–16. https://doi.org/10.1016/j.pepi.2017.09.002

Yu, W.-C., & Wen, L. (2006a). Inner core attenuation anisotropy. *Earth and Planetary Science Letters*, *245*, 581–594. https://doi.org/10.1016/j.epsl.2006.03.043

Yu, W.-C., & Wen, L. (2006b). Seismic velocity and attenuation structures in the top 400 km of the Earth's inner core along equatorial paths. *Journal of Geophysical Research*, *111*, B07308. https://doi.org/10.1029/2005JB003995

Yu, W.-C., & Wen, L. (2007). Complex seismic anisotropy in the top of the Earth's inner core beneath Africa. *Journal of Geophysical Research*, *112*, B08304. https://doi.org/10.1029/2006JB004868

Zheng, Y., & Wu, R.-S. (2008). Theory of transmission fluctuations in random media with a depth-dependent background velocity structure. *Advances in Geophysics*, *50*, 21–41. https://doi.org/10.1016/S0065-2687(08)00002-2